NASA Technical Memorandum 112855
U. S. Army Research Laboratory Technical Report 1423

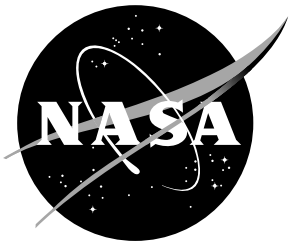

XV-15 Structural-Acoustic Data

Karen H. Lyle
Vehicle Technology Center
U.S. Army Research Laboratory
Langley Research Center, Hampton, Virginia

June 1997

National Aeronautics and
Space Administration
Langley Research Center
Hampton, Virginia 23681-0001

XV-15 Structural-Acoustic Data

Karen H. Lyle

Introduction

Use of tiltrotor aircraft has become a viable means of intercity travel. The tiltrotor is able to pick up passengers at the center of a city and then transport them relatively quickly to locations within a 500 kilometer radius. Thus in areas such as the Northeast, much of the transportation could be accomplished using one vehicle rather than a combination of fixed wing aircraft, helicopters and ground vehicles. In order for such vehicles to be commercially viable, the interior noise and vibration levels must be acceptable to the general public as passengers. Development of technology to make tiltrotor interiors quiet is part of the interior noise component of the NASA Advanced Subsonic Technology Program. A review of the literature revealed very little structural-acoustic data related to the tiltrotor and more specifically to the XV-15. Shank[1] reported that the untreated tiltrotor interior noise levels are comparable to helicopters for hover; however, in forward flight the tiltrotor is somewhat quieter than helicopters. In addition to the data presented by Shank, a memo written by Maisal[2] includes exterior spectrum levels measured on the surface of the XV-15 at four positions. The memo not only includes information on hover and level flight but also for various nacelle angles. In addition, information regarding the repeatability of the measurements was included. However, these data are not formally documented or generally available. Additional data are necessary to better understand the physical mechanisms that produce the structural vibrations and interior noise in the tiltrotor. For this reason, structural-acoustic measurements were taken aboard an XV-15 aircraft and are presented in this paper. The measurements included exterior surface pressures, structural accelerations and interior pressures. The flight conditions included both level flight in airplane mode (nacelle at 0 degrees) and out-of-ground-effect (OGE) hover in helicopter mode (nacelle at 90 degrees). The data were also acquired to validate prediction codes capable of accurately predicting the exterior pressure on the fuselage. However, comparisons of predicted and measured data will not be included in this paper.

Experimental Set-up

A photograph of the XV-15 is shown in Figure 1. The XV-15 is a prototype tiltrotor (three-bladed propeller) with overall cabin dimensions of approximately 4.0 x 1.4 x 1.4 m. An aircraft cabin of this size would accommodate 6-8 passengers. This particular aircraft was built in the early 1980's as a proof-of-concept for tiltrotor technology. The aircraft interior was green, i.e., no trim. A large auxiliary fuel tank occupies approximately one-quarter of the fuselage cabin. In addition to the auxiliary fuel tank, various recording and monitoring equipment is contained in the cabin. Due to the atypical cabin interior for this particular aircraft, the measurements presented in this report were focused on the exterior pressure loading on the fuselage rather than interior noise.

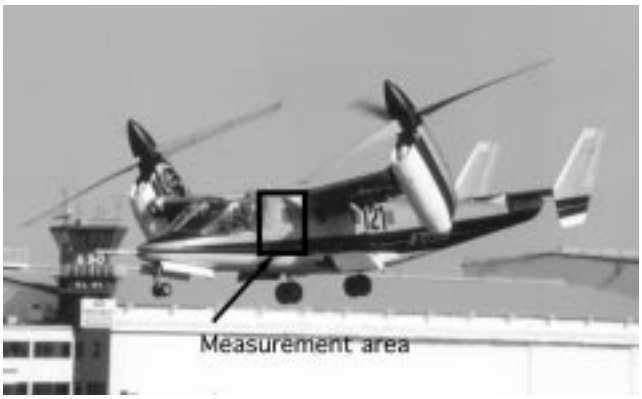

Figure 1 Photograph of XV-15.

A photo indicating the transducer locations is shown in Figure 2 (Coordinates for all transducer locations are listed in Table I). A sketch of the fuselage with dimensions has been included as Figure 3. These transducer locations form a "T" centered about Position A which was assumed apriori to be the closest approach of the propeller to the starboard side of the fuselage during airplane mode. However, following the data reduction, the closest approach appears to be between locations A and E. Position D was located near the wing fairing. Position F was at the top center of the fuselage and would presumably see equal contributions

from both rotors. The two rotors are mechanically linked so that they rotate at exactly the same rate. This eliminates any 'beating' in the signals but also eliminates the capability to distinguish the response of the two rotors. Two exterior pressure transducers (located at positions I and J) failed during the flight and thus data for those positions will not be presented.

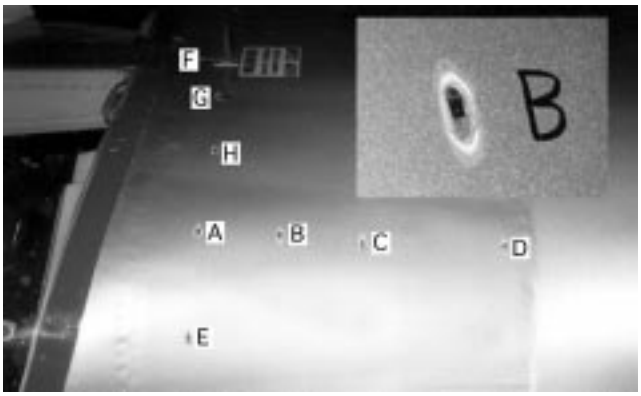

Figure 2 Photograph of exterior sensor locations .

Table I Transducer locations and separation distances (d) , in meters.

Location	Station-Line (SL)	Butt-Line (BL)	Water-Line (WL)	d
A	6.18	0.610	2.41	0
B	6.32	0.597	2.40	0.13
C	6.45	0.584	2.39	0.26
D	6.69	0.572	2.37	0.50
E	6.18	0.737	2.31	0.16
F	6.12	0.0	2.46	0.61
G	6.17	0.184	2.46	0.42
H	6.18	0.394	2.45	0.21
K	6.18	0.800	1.08	1.35
L	6.32	0.127	2.08	-

The exterior pressures were measured at nine locations using surface mounted pressure transducers with 1.88 mm diameter diaphragms. The surface mount resulted in the transducer protruding approximately 1.5 mm from the skin (Figure 2 inset). For the flight speeds presented here and the fact that the primary noise is from the rotating blades, this offset into the flow was not considered critical. These exterior pressure sensors measured differential pressures and were vented to the aircraft interior. The transducers were rated to +/- 3450 Pa (differential) with a nominal sensitivity of 0.000261 mV/Pa/Vin. For this test the excitation voltage was 12 V. A signal conditioner provided a gain of 1100 to assure adequate input to the tape recorder. The static pressure differential was confirmed to be sufficiently low during post data analysis.

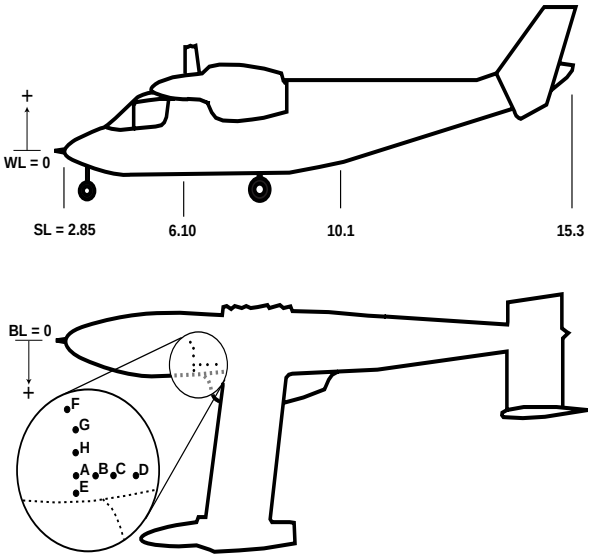

Figure 3 Diagram of XV-15 fuselage.

Accelerations were measured on the inside of the skin at 5 locations (A, B, C, E, and H) using lightweight accelerometers with a sensitivity of 10 mV/g. The interior transducers at position B are shown in Figure 4. Each accelerometer was essentially collocated with an exterior pressure sensor. These very lightweight accelerometers, 0.4 grams, were selected to minimize the effect of the accelerometer mass on the structure. The locations were selected sufficiently far from any stiffeners to assure adequate acceleration response. Signal conditioning of the acceleration signals provided a gain of 10 for recording.

Interior pressures at two locations were measured using half-inch condenser microphones. Following amplification, the signal to the tape recorder was 105 Pa/V. One microphone was positioned in the acoustic nearfield of the fuselage sidewall, .025 m inboard from position B. The second microphone was near the propeller plane near a typical passenger head-height and 0.3 m from the forward bulkhead (Position L).

One minute of data were acquired at the six flight conditions indicated in Table II. The transducer signals as well as the rotor tach signal were recorded on a 32-channel digital tape recorder at a sampling rate of 5 kHz. The data were then downloaded to a computer workstation for data reduction and analysis. One hundred fifteen onboard data parameters were simultaneously recorded for correlation with the transducer data via the time code.

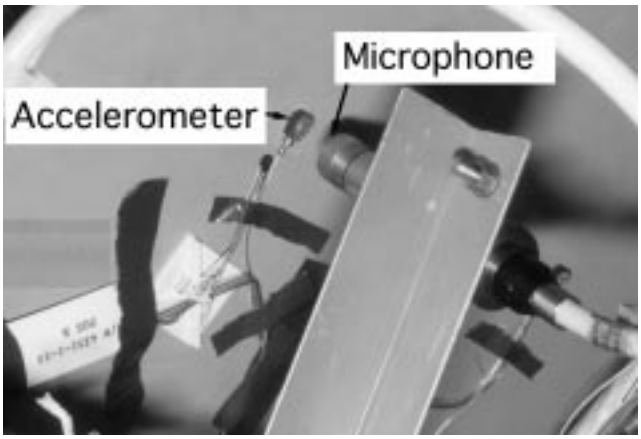

Figure 4 Photograph interior transducers at location B.

Table II Test flight conditions.

Condition	*Nacelle angle (degrees)*	*Speed, m/s (knots)*	*RPM (nominal)*
I	0	72.0 (140)	522
II	0	82.2 (160)	522
III	0	92.5 (180)	522
IV	0	103.(200)	522
V	0	113 (220)	522
VI	90	Hover (OGE)	608

Results

Overall Level Summary

The overall RMS levels for the exterior pressure transducers, accelerometers and microphones are shown in Figures 5-7, respectively. For each figure, the overall levels are plotted as a function of measurement locations, with the six flight conditions indicated by the various symbols. In each of the figures, note that as the flight speed increases from 72 m/s (Condition I) to 113 m/s (Condition VI), the overall level also increases. As will be seen in the Autospectral Summary section, the overall levels for exterior pressures, accelerations and interior pressures have dominant components in different frequency ranges of the spectra.

For Figure 5, the increase in exterior SPL, as the speed changes form 72 to 113 m/s, ranges from 5 dB at Location F to 10 dB at Location A. The exterior SPL in hover is generally less than or equal to the SPL for Condition I for those measurement locations in the tip path plane (E through K). The SPL at position K for hover is 6 dB less than that for Condition I. For Position K, the propeller is rotating much farther from this location during hover than for forward flight in airplane mode. However, for the positions located to the aft of the tip path plane, the hover condition is nearer the higher flight speeds. Exterior data acquired by Maisal (4 locations aft of the tip path plane) indicated that the hover data levels are nearly the same as those for forward flight at the higher speeds. Similar trends are evident here where the level in hover for locations B and C is within 1 dB of that acquired at 113 m/s and for location D it is within 2 dB.

For the acceleration measurements, see Figure 6, the spread in overall level for airplane mode ranges from 3 dB at Position A to 6 dB at Position H. Unlike the exterior pressure measurements, the acceleration levels for hover are within 1 dB of Condition I for all locations. The overall acceleration levels will be shown later to be dominated by higher frequencies and not the blade passage frequencies.

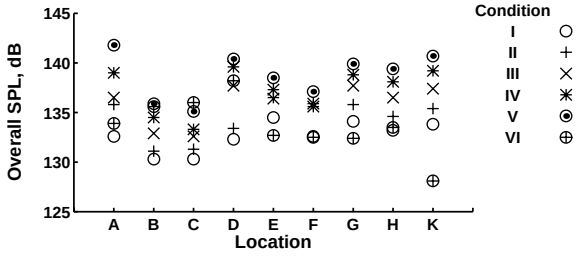

Figure 5 Overall exterior sound pressure levels.

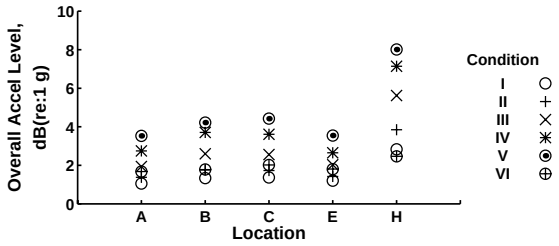

Figure 6 Overall acceleration levels.

The interior noise levels at both microphone locations, Figure 7, increase 4 dB as the forward flight speed increases. As for the acceleration levels, the hover data are within 2 dB of that for Condition I. A comparison of A-weighted SPLs for level flight in airplane mode between microphone location L and data acquired by Shank is shown in Figure 8. The Shank data are an average of pressures from 6 microphones placed throughout the cabin at approximate passenger head height. The agreement between the two sets is good. Shank also reports that the response in hover is nearly equal to that at the higher flight speeds. The reason for the discrepancy between this set of

data and that reported by Shank has not been determined. Maisal did indicate that the variance was greater for the exterior pressures in hover than for the level flight cases. Also, in comparing the data in Figure 7 for Position L with that in Figure 8, A-weighting the spectra changes the relative importance of the hover level when compared with forward flight data.

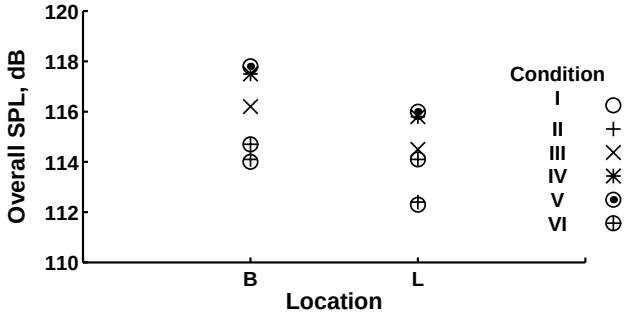

Figure 7 Overall interior sound pressure levels.

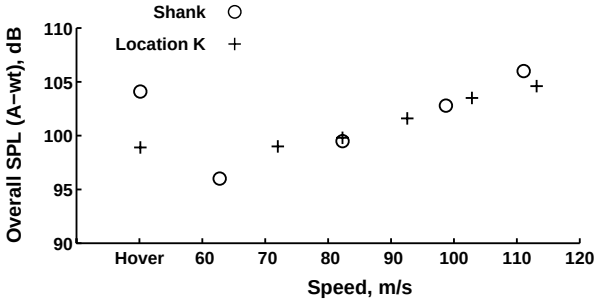

Figure 8 Comparison of A-weighted overall sound pressure levels at Location K with Shank data.

Time History Summary

Sample time histories for each transducer at three flight conditions are shown in Figures 9-17. The time period represents one rotation of the propeller. The thin line in each figure, is a representative instantaneous response while the time averaged response (based on 75 ensembles of exactly the same rotation period) is indicated by the heavy line. Special care had to be taken in time averaging the data for airplane mode. The time average was based on the 1/rev tach signal. The shaft rotation for airplane mode varied erratically up to 3.5 % over the one minute sampling period, while the shaft rotation varied significantly less (up to 0.35 %) for the aircraft in hover. This variability in shaft rotation has been verified by the aircraft manufacturer and is not an anomaly resulting from the data acquisition or reduction. Note that the tach signal was sampled at 5 kHz which could result in a 0.35 % uncertainty due to the digital sampling. This uncertainty would produce a 0.627 degree error in rotor azimuth angle. At the exterior pressure sensors, the time averaged response closely follows the instantaneous response, Figures 9-11, for Conditions II, IV and VI, respectively. In comparing the data for Conditions II and IV, the effect of forward flight changes the magnitude of the response but does not significantly change the shape of the time history. The time history response does vary significantly as a function of spatial location. Thus the response at position A is very different from that at position E, although these points are separated by less than 0.2 m. The character of the response in hover is very different from that in forward flight. For hover, the shape of the time history is much less dependent on the spatial location. The difference between time-averaged and instantaneous responses at Position D is an indication of the instability of the response during hover. This instability is not a result of variations in the rotor speed, but more likely results from unsteady flight conditions, such as wind gusts.

For the acceleration responses, Figures 12-14, the time averaged response is much less than the instantaneous response. This indicates that much of the acceleration is not coherent with the rotating blades. Later sections of this report will include coherence values. For level flight, indication of the blade passage can be seen at approximately 0.015, 0.055, and 0.095 seconds for Condition II (Figure 12), and approximately 0.02, 0.06, and 0.10 seconds for Condition IV (Figure 13). The response at location H is much greater than the other positions. For hover, Figure 14, the time averaged response appears to be nearly a straight line. The passage of the blades is not readily evident in the response, even when the ordinate scale is considerably expanded.

The time averaged interior microphone responses, Figures 15-17, closely correspond to the instantaneous responses. The passage of the three blades during the period of rotation is clearly seen. Again, the shape of the response is not greatly dependent on forward flight speed. A double pulse appears for forward flight as the blade passes. The source of such a response could be ringing of the structure or the difference in arrival time of the pressure pulse from the two rotors. The response in hover, Figure 17, is significantly different from that in forward flight. However, these responses are similar in characteristic to that of the exterior pressure transducers, Figure 11.

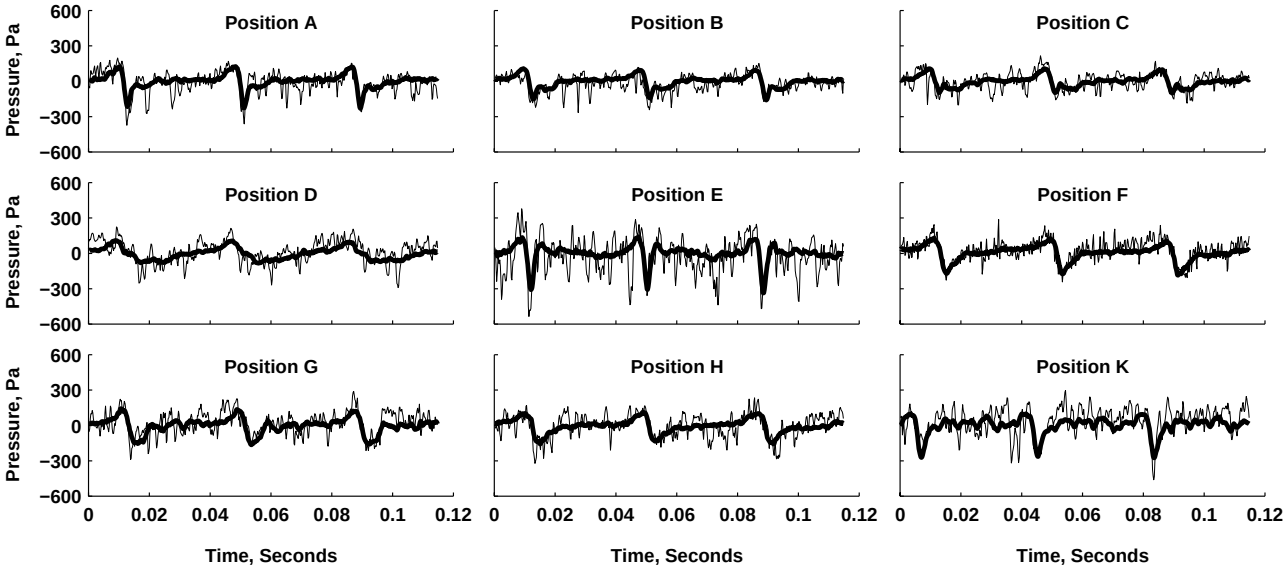

Figure 9 Exterior pressure time histories for Condition II.

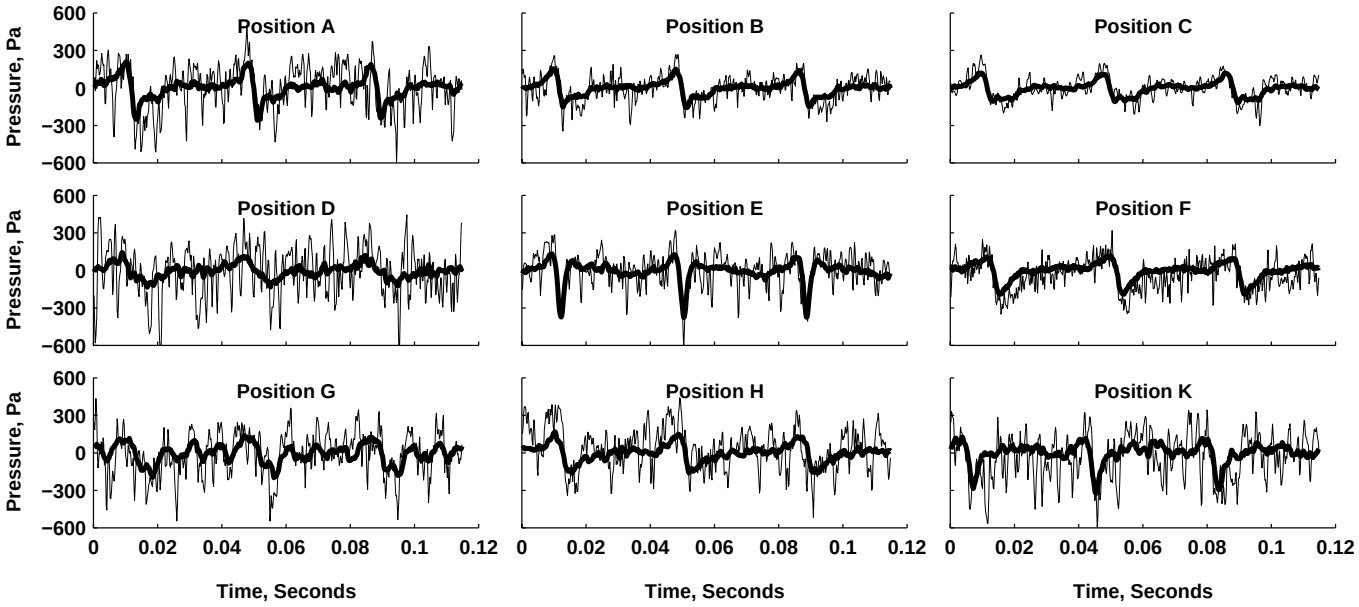

Figure 10 Exterior pressure time histories for Condition IV.

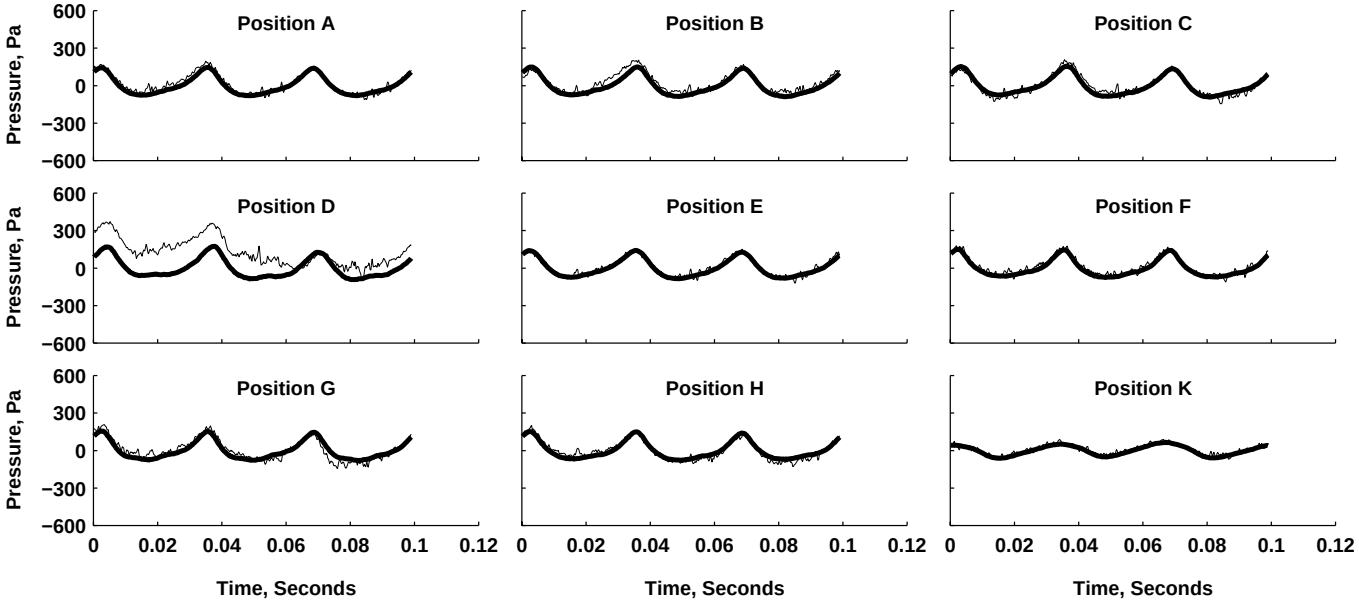

Figure 11 Exterior pressure time histories for Condition VI.

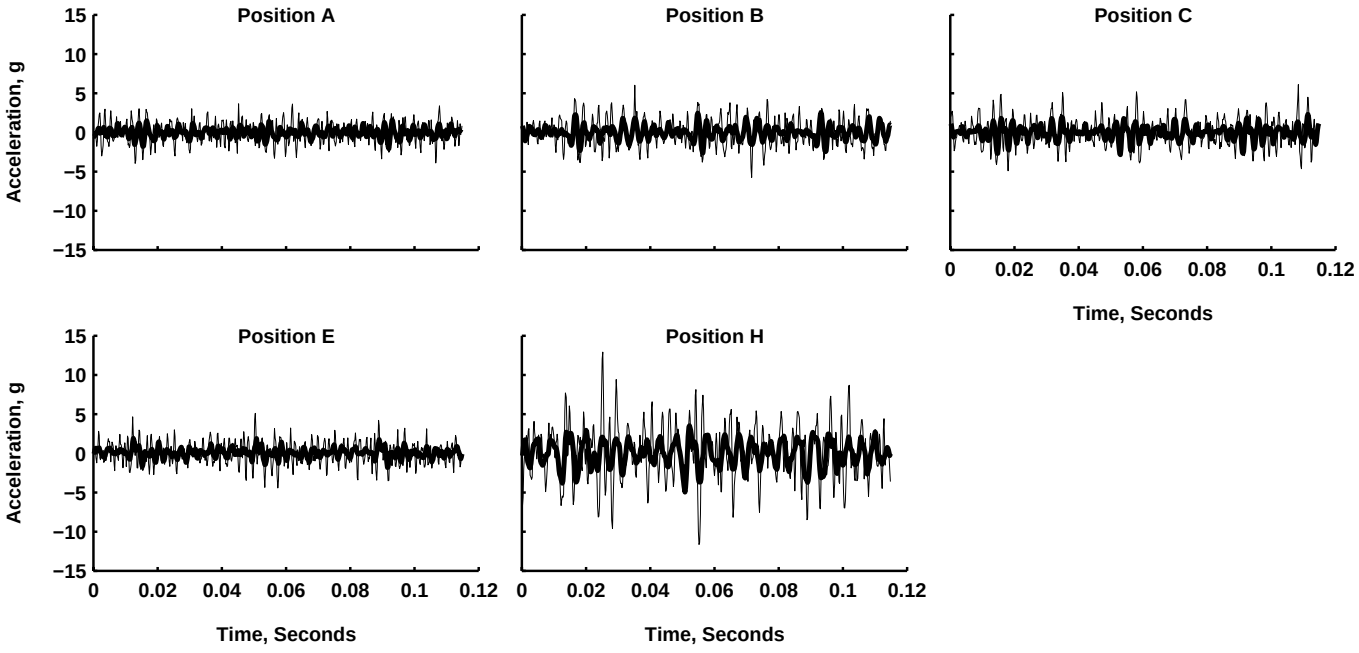

Figure 12 Acceleration time histories for Condition II.

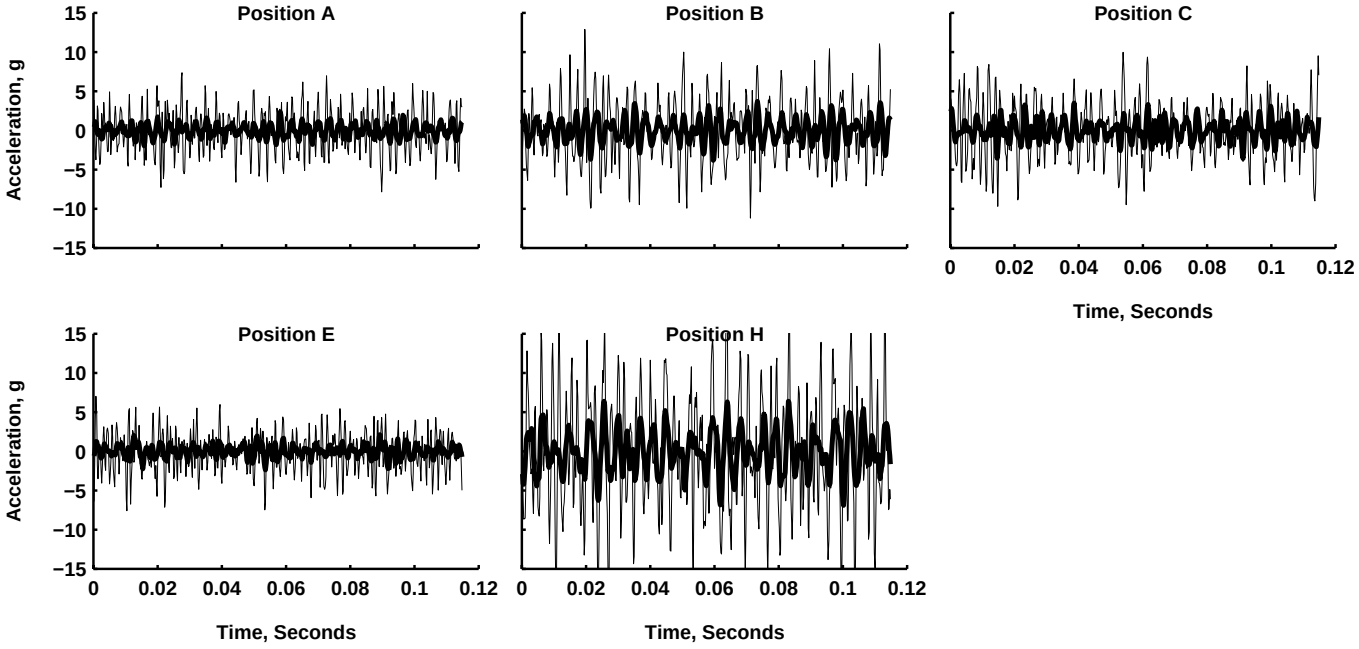

Figure 13 Acceleration time histories for Condition IV.

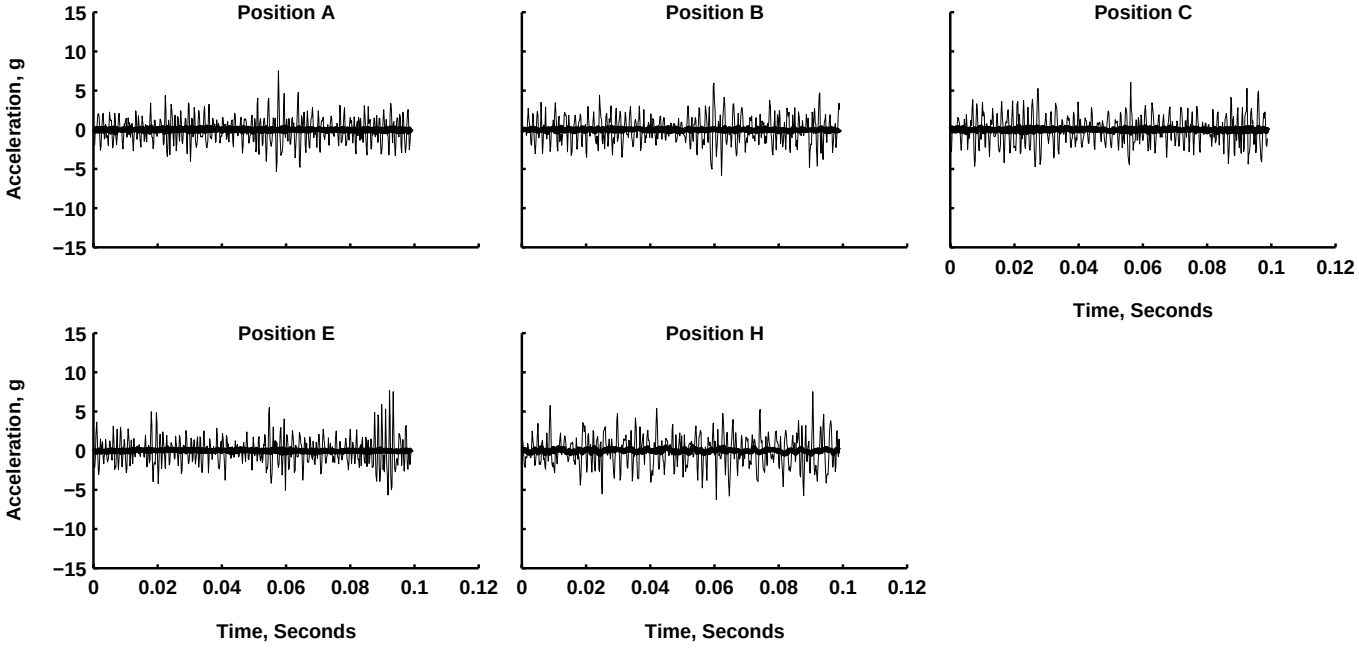

Figure 14 Acceleration time histories for Condition VI.

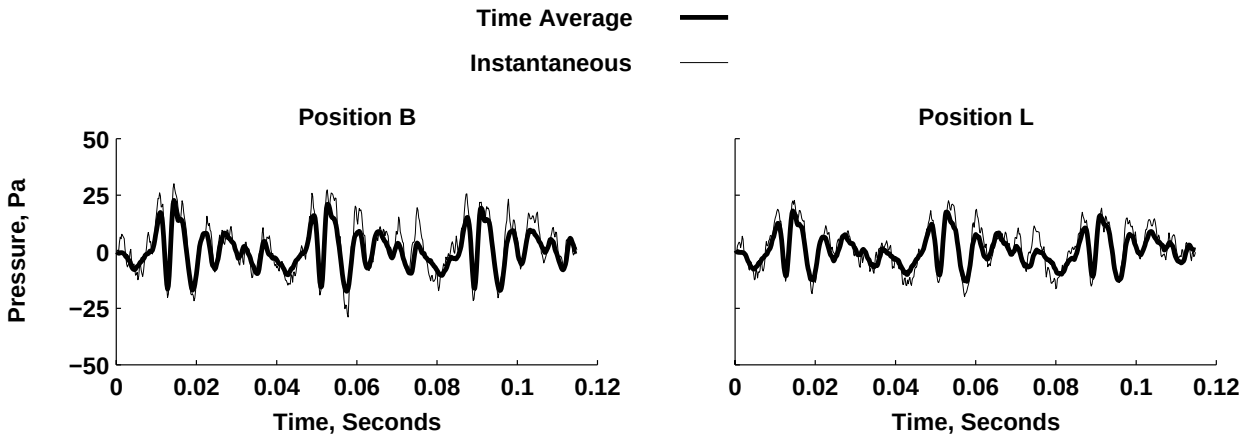

Figure 15 Interior pressure time histories for Condition II.

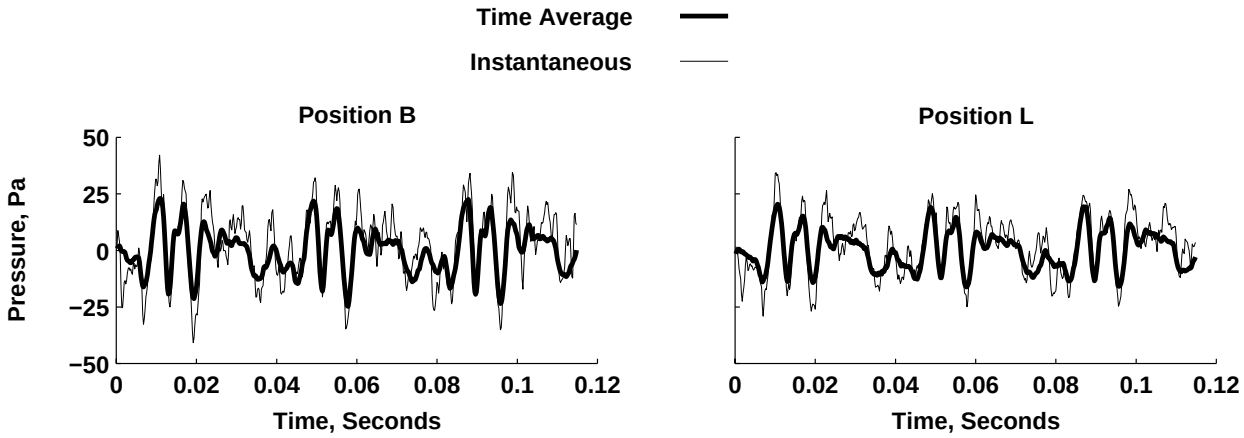

Figure 16 Interior pressure time histories for Condition IV.

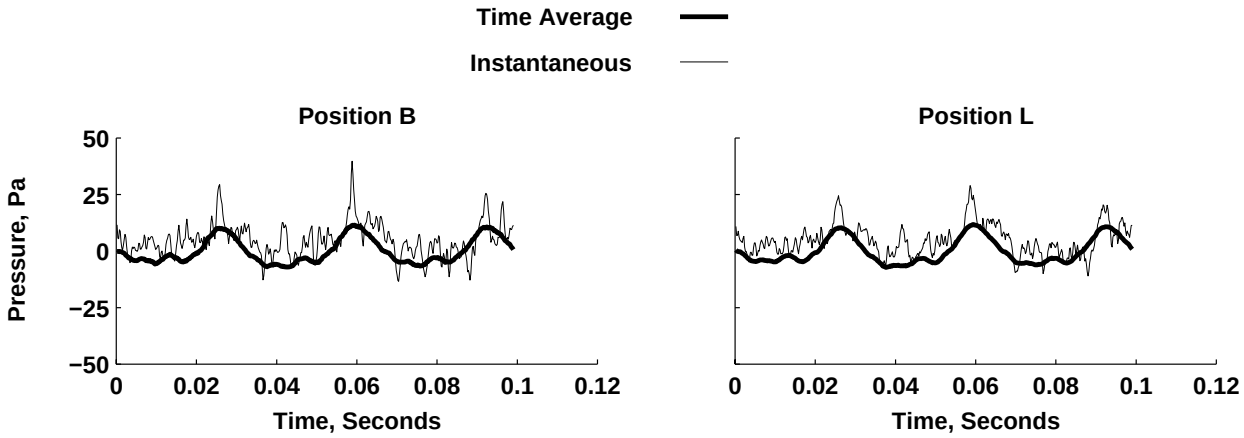

Figure 17 Interior pressure time histories for Condition VI.

Autospectral Summary

Sample autospectra for Conditions II, IV and VI are presented in Figures 18-26. The fundamental blade passage frequency (BPF) is 26.1 Hz in airplane mode and 30.4 Hz in hover. To center the BPF frequencies in the analysis bands, the data for airplane mode were analyzed with a 1.74 Hz bandwidth while those for hover were analyzed using a 2.03 Hz bandwidth. Although the tach period varied significantly for level flight, the data for level flight conditions (I-V) were found to be stationary over the 1 minute recording period. On the contrary, the tach period for hover was relatively constant, while the data for hover were not stationary. The autospectra presented in this section were calculated based on the entire 1 minute of data. A sample autospectra for the tach signal is given in Figure 18. Note that all harmonics of the shaft rotation appear. The harmonics of the blade passage frequency have been highlighted by circles.

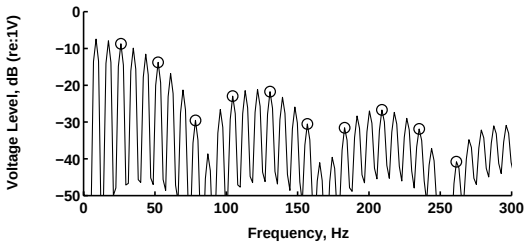

Figure 18 Autospectra of tach signal for Condition II.

In general, the harmonic peaks of the exterior pressures due to the rotating propeller approaches the broadband noise floor between 250 - 300 Hz (Figures 19-20). For the data at position D, located near the wing fairing, only the first 3 harmonics of the BPF are greater than the broadband noise. At this location the wing fairing significantly disturbs the flow and presumably increases the broadband level. Secondly, the response at the harmonics decreases much more rapidly as frequency increases than for the other locations. The pressure at Position E has a greatly reduced response at the BPF for the level flight conditions compared to the other locations.

The peaks in the spectra at 400 and 800 Hz are attributed to electrical sources powered at 120V and 400 Hz. The peak at 790 Hz is seen in all flight conditions. It becomes more apparent during hover where the broadband noise floor at the high frequencies is lower. Since the frequency does not change with blade rotation rate (i.e., occurs for hover and forward flight), the source is not produced by the rotating blade.

Like the time histories, the spectral shape is very dependent on spatial location, however, the forward flight speed primarily influences spectral amplitude, but not the spectral shape. A-weighted spectra would cause the responses at the lower frequencies to have much smaller amplitudes than those at the higher frequencies. However, the lower frequencies can still cause annoyance to passengers. The high frequency response is assumed to be primarily composed of the flow generated noise. When comparing Figures 19 and 20, the background spectral levels are much higher for locations A, B, D, G, H and K, as the flight speed increases.

In hover the spectral shapes are considerably different (Figure 21), as would be expected from the time histories. The SPL decays exponentially as a function of frequency for the first few harmonics. Also note, that although the response at the BPF for position E was noticeably lower for forward flight, no such behavior is observed during hover. Peaks at 967 Hz are seen in all three transducer types during hover. This frequency is 95.5 times the blade rotation rate of 10.13 Hz. Since this spike exists in all the data channels, but only during hover, it is not considered to be an electrical anomaly in the data acquisition system. Although the source is not known, this phenomenon could be related to a gear meshing frequency.

The acceleration autospectra (re: 1g), Figures 22-24, have qualitatively the same shape at all measurement positions. They contain considerable high frequency energy; however, the BPF harmonics dominate the background noise at the lower frequencies in all cases. For position E, note that the response at the 2nd harmonic is 15 to 20 dB less than the response at either the 1st or 3rd harmonics for both forward flight conditions. In many cases the tenth harmonic (near 260 Hz) is the largest. The broadband levels above 400 Hz increase approximately 10 dB from Condition II to Condition IV.

As was evident from the time-averaged time histories for the hover condition, the spectra are dominated by the high frequencies. The responses at the first few BPF harmonics for hover are 10 dB lower than the corresponding results for forward flight.

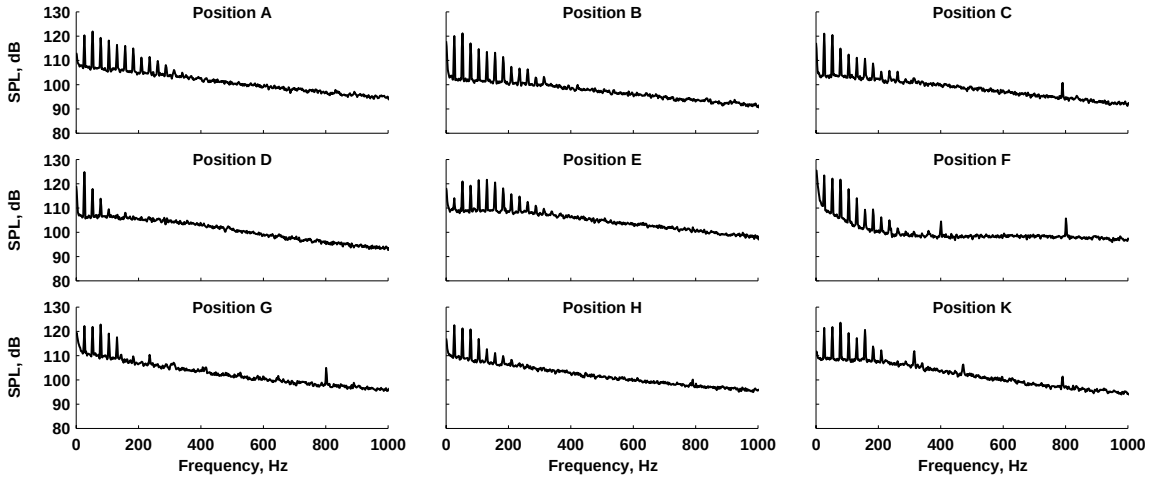

Figure 19 Exterior pressure autospectra for Condition II.

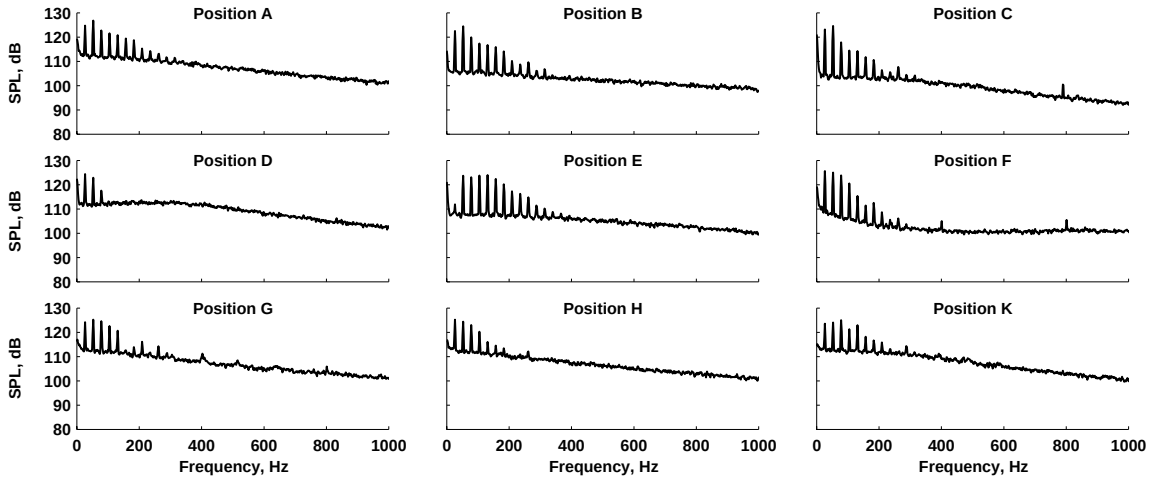

Figure 20 Exterior pressure autospectra for Condition IV.

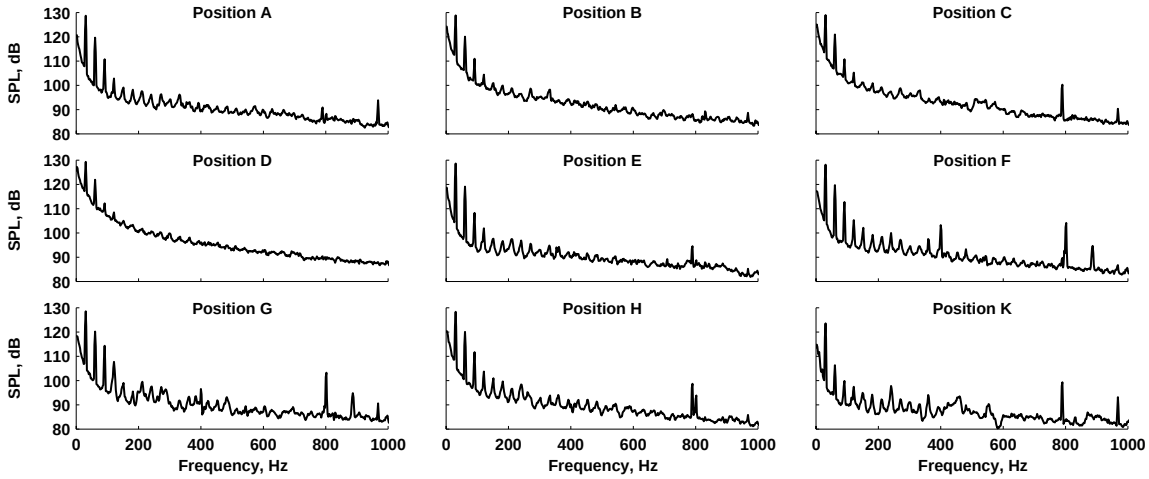

Figure 21 Exterior pressure autospectra for Condition VI.

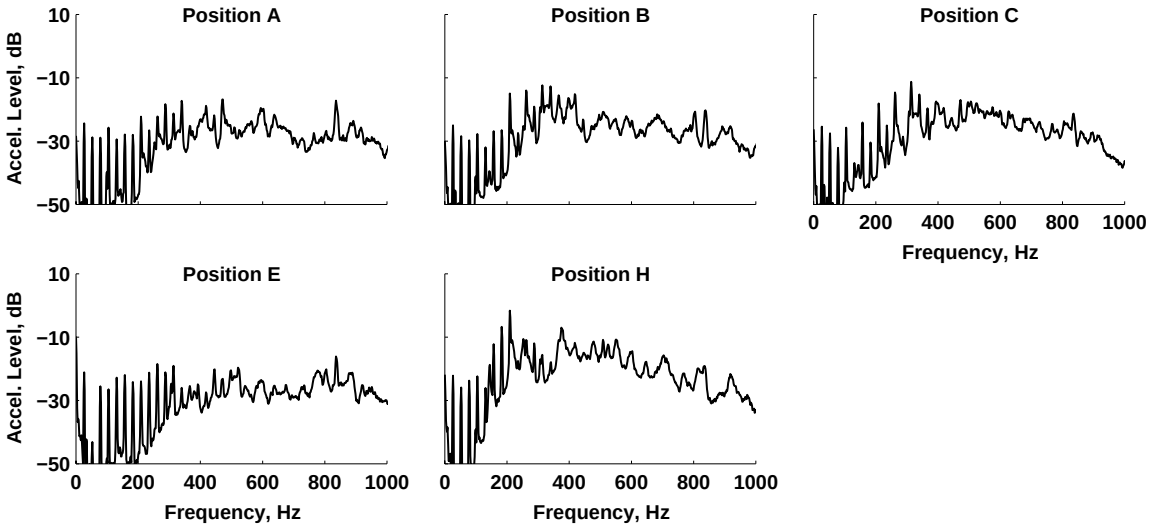

Figure 22 Acceleration autospectra for Condition II.

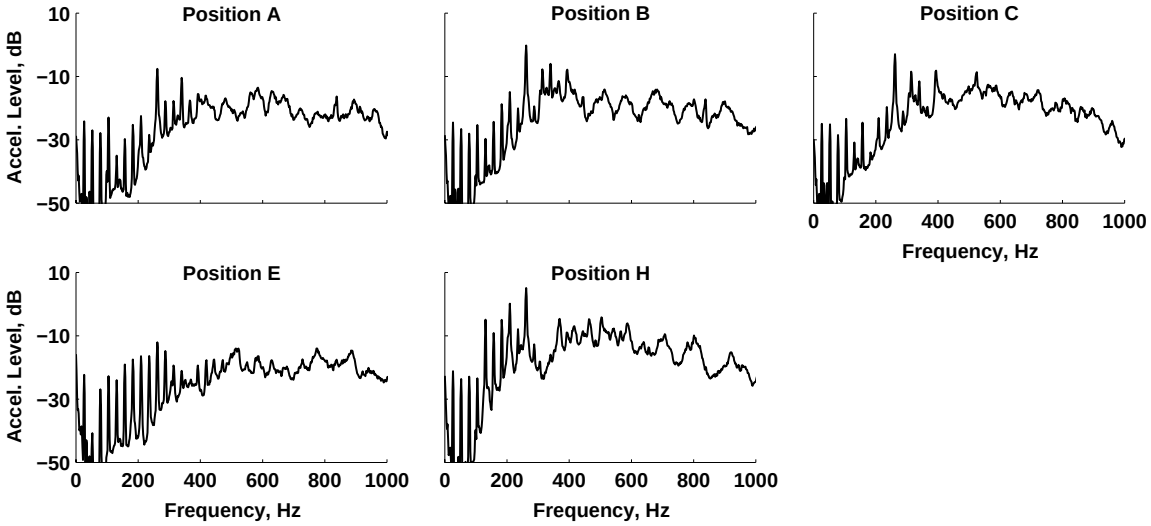

Figure 23 Acceleration autospectra for Condition IV.

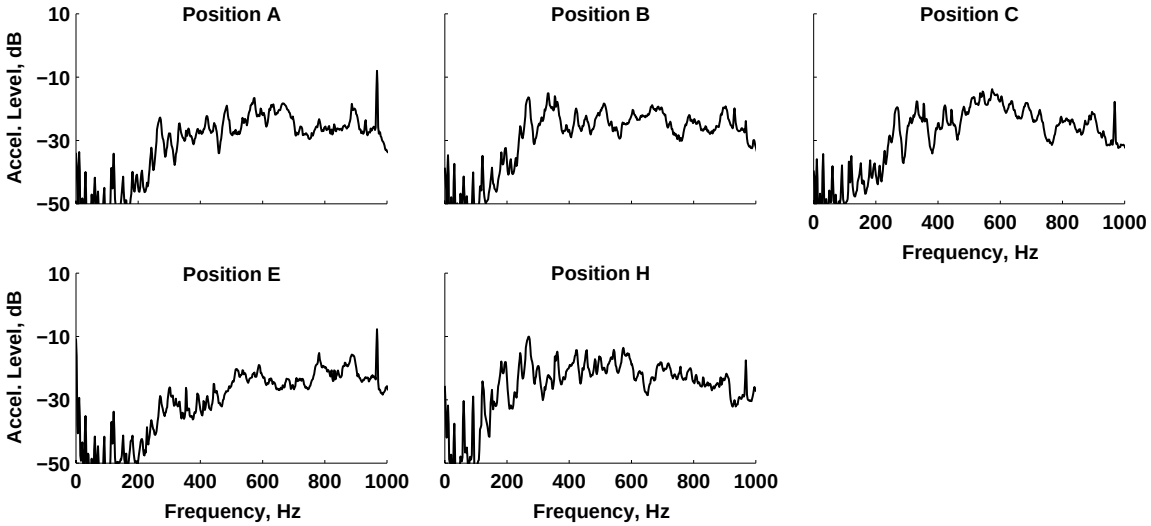

Figure 24 Acceleration autospectra for Condition VI.

The autospectra for the two interior pressure locations are shown in Figures 25-27. As indicated in the introduction, these flight data were acquired to increase the understanding of the physical phenomena that contribute significantly to the interior noise. However, due to the atypical interior configuration, the interior noise data will be used to identify the frequency range of interest. For positions B and L, both the unweighted and A-weighted spectra are dominated by frequencies up to the tenth harmonic. It is noteworthy that the elevated high frequency spectral levels measured by the exterior sensors as well as the accelerometers do not couple well to the interior space. This may be due to spatially incoherent noise sources on the exterior of the structure. For this reason, the data reduction will concentrate on the first 10 harmonics.

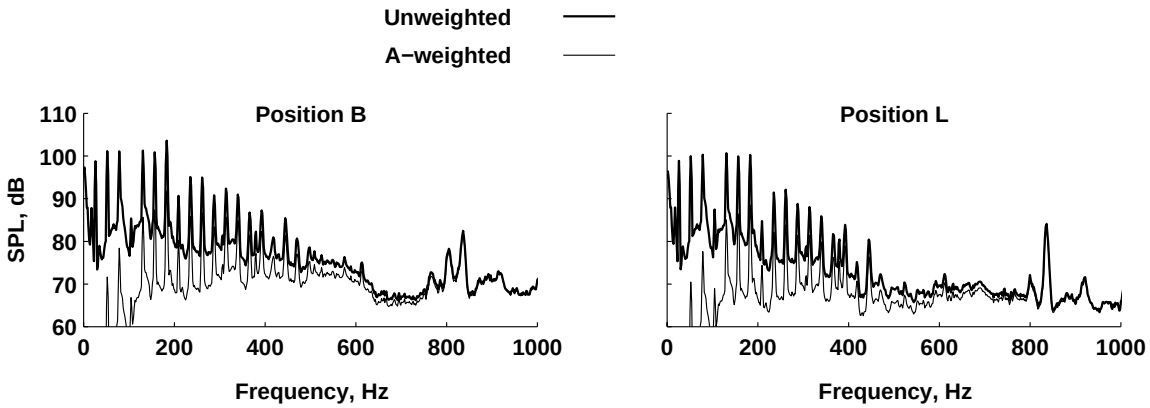

Figure 25 Interior pressure autospectra for Condition II.

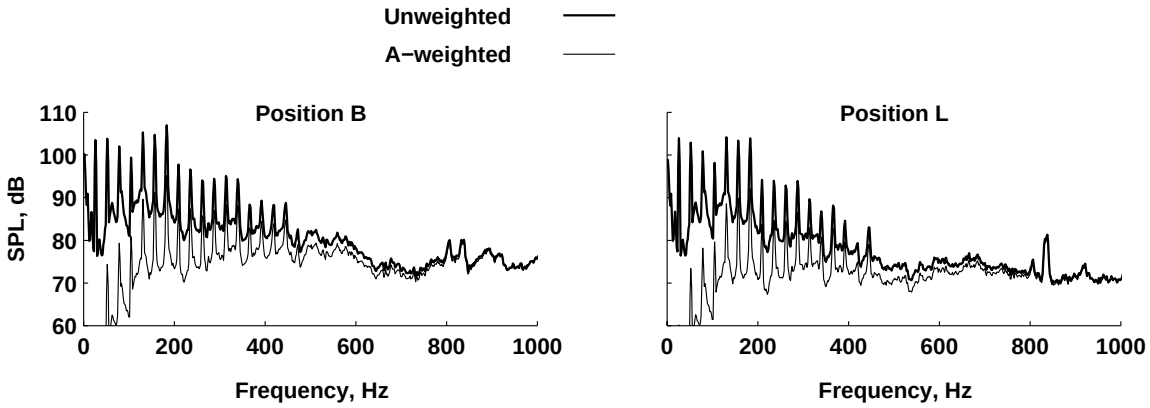

Figure 26 Interior pressure autospectra for Condition IV.

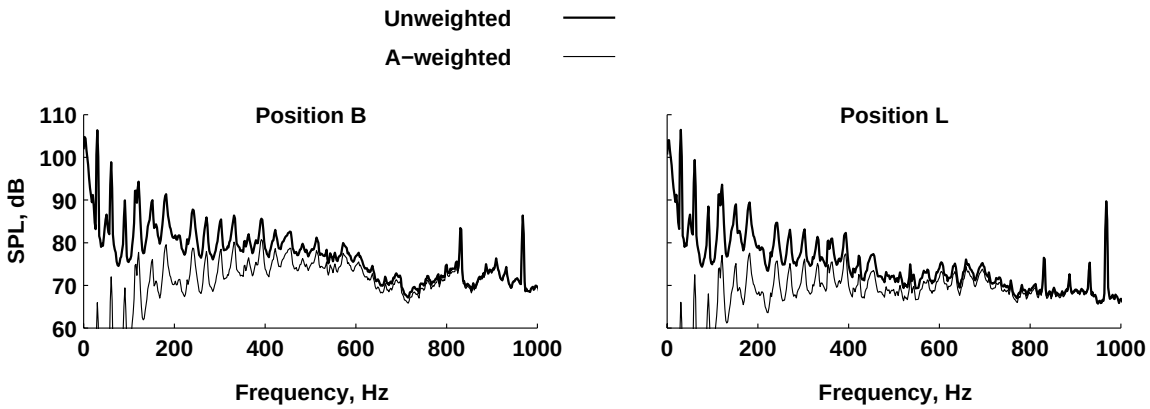

Figure 27 Interior pressure autospectra for Condition VI.

Coherence Summary

The coherence between the various sensors and the tach signal for the harmonics up to 300 Hz have been plotted in Figures 28-33. Since the tach signal contains only harmonics of the rotation frequency, data are only shown at harmonics of the BPF. The forward flight data have been separated from that for hover to minimize clutter and to emphasize data trends in the figures. These coherence values can be utilized to ascertain the validity of the values presented in the remainder of the paper.

In general, the coherence values of the exterior pressures relative to the tach signal, Figure 28, are acceptable (> 0.5) at all the locations. Position E, which has been noted previously as having an unusually low signal to noise ratio at the BPF, also has a marginal to low coherence value at the BPF. The coherence values for Position D drop considerably above the third harmonic. Based on these results, the spectral values for Position D at the harmonics above the third are not related to the rotor excitation.

For hover, Figure 29, the coherence is only good up to the third harmonic for most locations. For some locations, such as C or K, the coherence values above the second harmonic would indicate that much of the energy is not related to the rotating propeller.

For the accelerations, the coherence values for forward flight are generally good except at Position C where considerable scatter occurs past the fourth harmonic (Figure 30). As an example of how the coherences could aid in further data reduction, consider Position A. The high coherence at the fifth harmonic for Conditions I, II and III shows that these signals are well correlated with the tach signal. On the other hand, for Conditions IV and V, the coherence is poor. Thus if using the data to validate a rotor prediction code, the data for Conditions I, II, and III would be considered reliable, but that for Conditions IV and V would not. For hover the coherence is poor over much of the frequency range indicating that the accelerations are not well correlated to the tach signal, see Figure 31.

The interior pressures are well correlated to the tach signal at many of the harmonics, Figures 32 and 33. The coherence for the ninth harmonic in both forward flight and hover for both of the microphone positions is low. In hover, the coherence across the frequency range at the two locations is nearly identical.

Sample narrowband coherence functions between the exterior pressures at Locations B, D, E and K and exterior pressures at Location A for Condition II are shown in Figure 34. For locations B and E, closest to A, the responses up to the sixth harmonic are well correlated to that at Position A. Note that for all cases the coherence at frequencies other than the harmonics is low - less than 0.1 and often much less. At the other extreme is Position D where the coherence at only the first two harmonics is greater than 0.8. The coherence at Position K (separated from Position A by 1.34 m) is considerably better than that for position D.

Sample narrowband coherence functions between collocated accelerometers and exterior pressure sensors for Condition II are shown in Figure 35. As for the data in Figure 34, the coherence at the non-harmonic frequencies is very low, typically much less than 0.1. The acceleration and pressure responses are generally well correlated at the first few harmonics. At position E, which was has been shown previously to have a higher acceleration response level than the other positions, the coherence is acceptable up to the tenth harmonic.

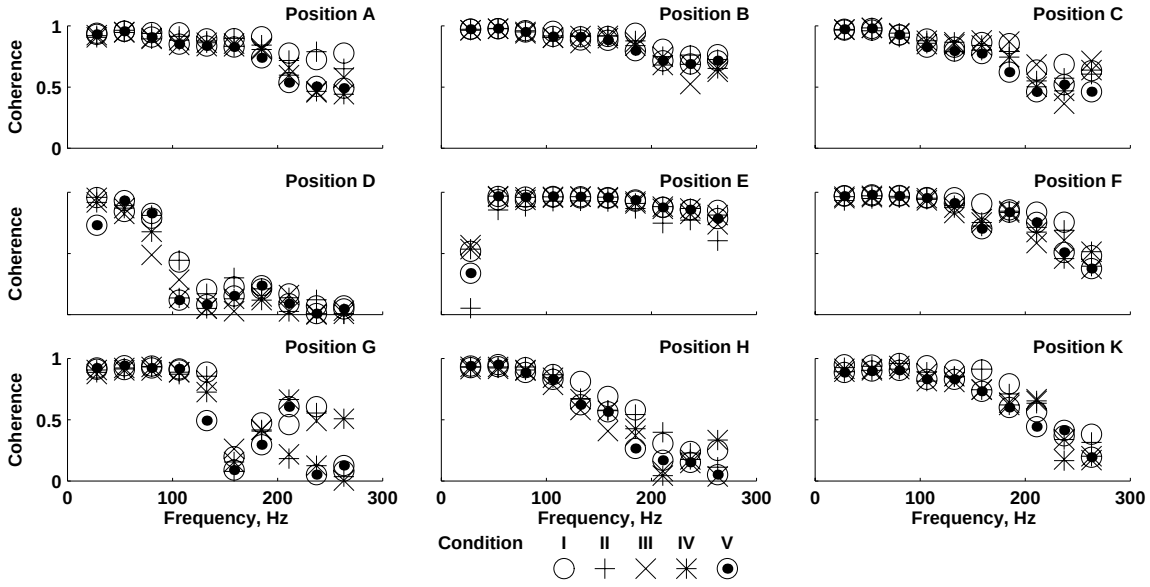

Figure 28 Coherence of exterior pressures relative to tach signal during forward flight.

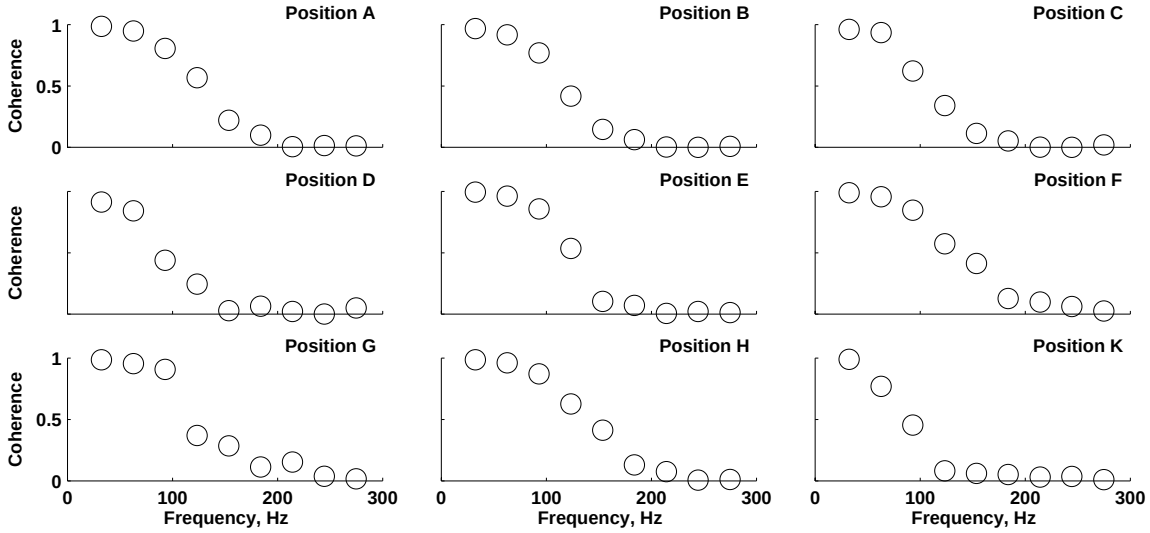

Figure 29 Coherence of exterior pressures relative to tach signal during hover.

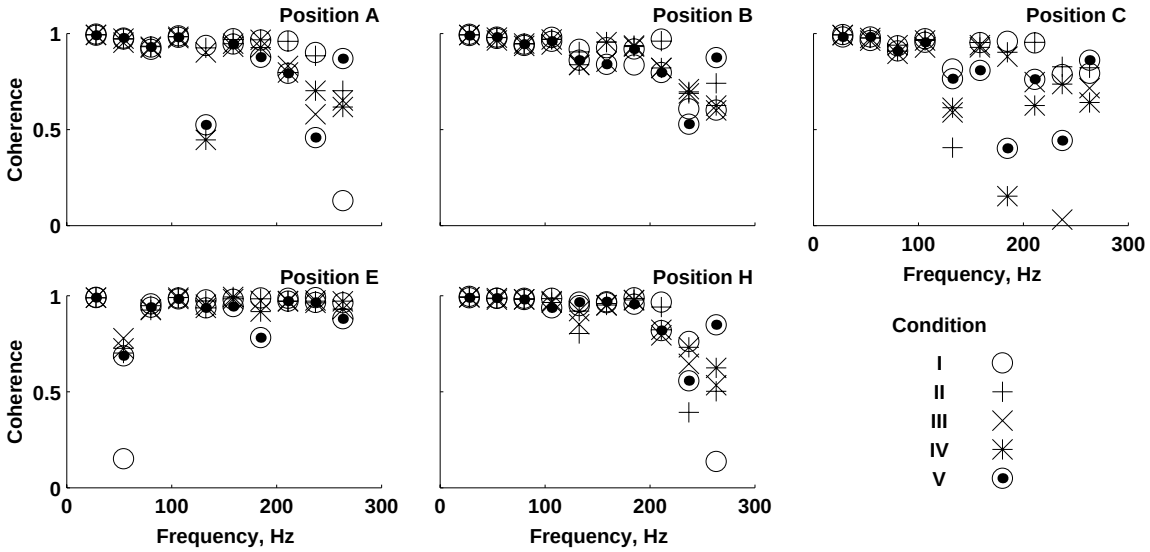

Figure 30 Coherence of accelerations relative to tach signal during forward flight.

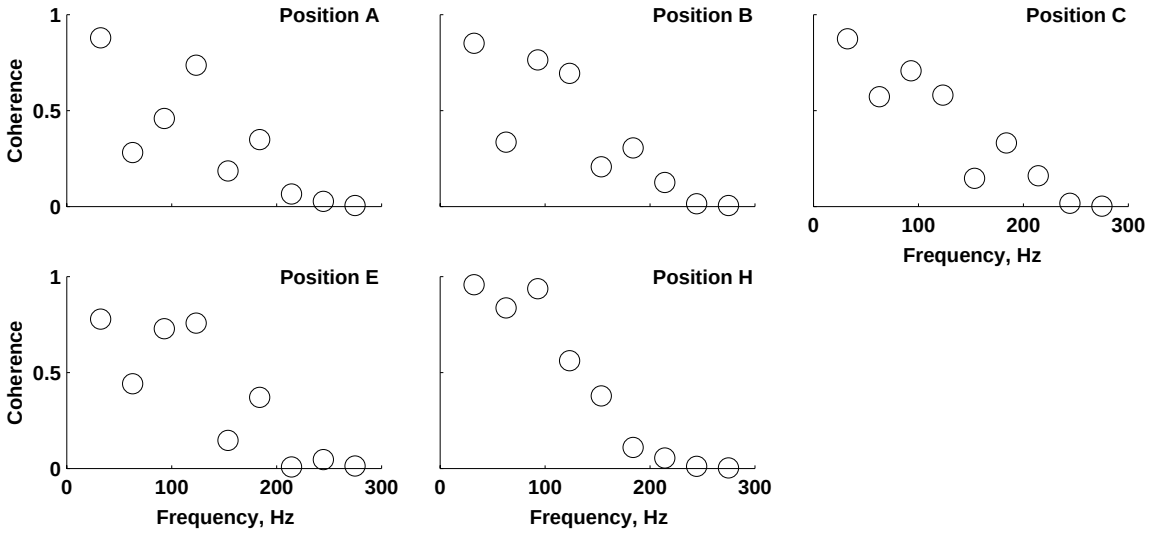

Figure 31 Coherence of accelerations relative to tach signal during hover.

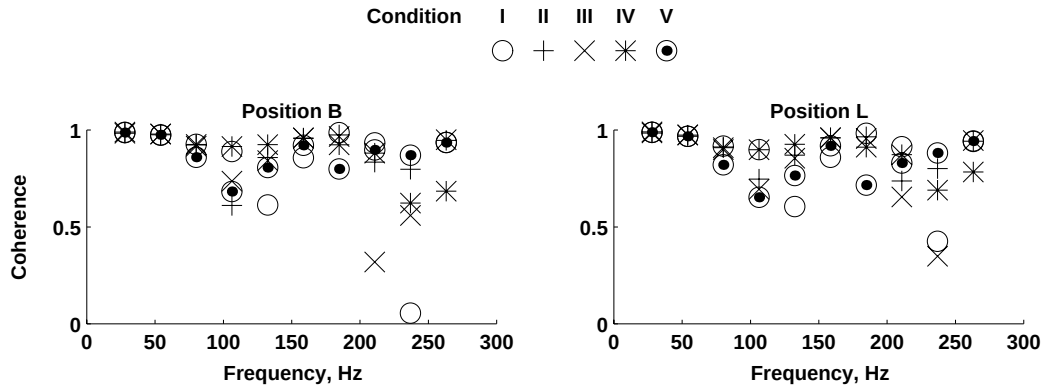

Figure 32 Coherence of interior pressures relative to tach signal during forward flight.

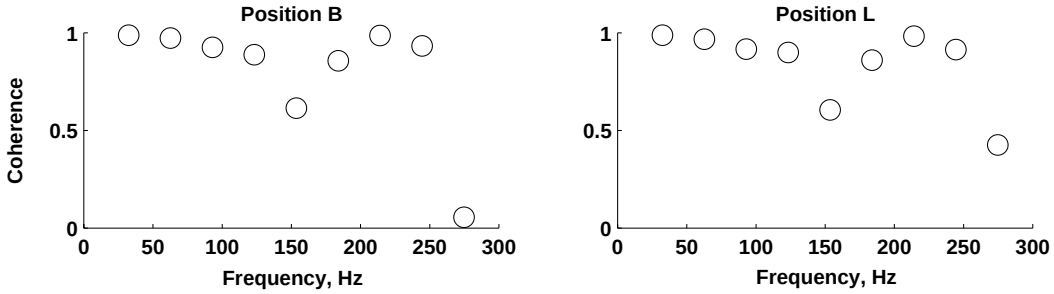

Figure 33 Coherence of interior pressures relative to tach signal during hover.

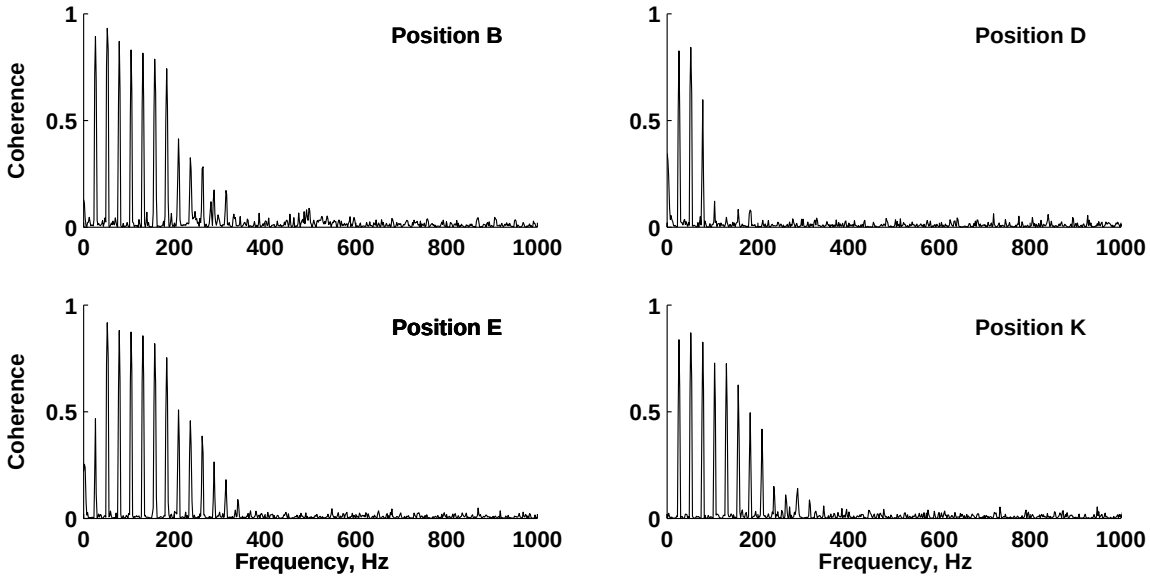

Figure 34 Coherence between exterior pressures relative to the exterior pressures at Location A.

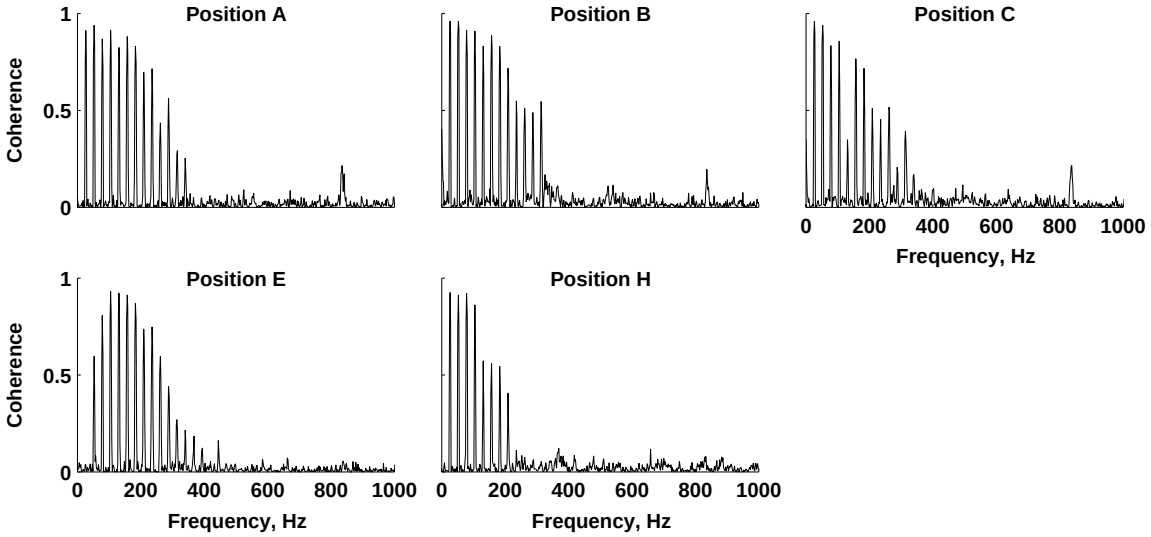

Figure 35 Sample narrowband coherences between collocated accelerometers and exterior pressure sensors.

Cross-Spectral Summary

The remainder of the data will be analyzed based on the time-averaged data such as that presented in Figures 9-17. It should be mentioned that the time histories were averaged based on shaft rotations of exactly the same period to eliminate data reduction error induced by the unsteady rotor rotation. The blade passage frequencies were selected based on the interior noise spectra results. The analysis frequencies were selected such that the harmonics were centered in an analysis bin which eliminated much of the leakage problem associated with applying windows (in this case a hanning window). As for the coherence values presented in the previous section, the data points for level flight have been included on one plot with those for hover on a second to minimize clutter in the figures. The level flight data generally collapse to very small scatter except at those harmonics where the signal to noise ratio is small or the associated coherence is low - resulting in less accurate cross-spectral values.

Exterior Pressure Transfer Functions

The magnitudes of the exterior pressure transfer function (TF) for Locations B through K relative to A for BPF harmonics up to 300 Hz are presented in Figures 36 and 37. The magnitude of the transfer function can be used to determine the closest approach of the rotor to the fuselage. When the magnitude of the transfer function of the pressure at Point X relative to the pressure at Point A is greater than 0 dB then the blade passes closer to point X than to point A. Conversely, when the magnitude is less than 0 dB then the pressure at Point A is greater than the pressure at Point X. For Figure 36, the various symbols refer to the 5 flight conditions (I-V) where the nacelle was in airplane mode. For these cases, the transfer function magnitude is not strongly dependent on the flight speed. Frequencies where large scatter in the data occurs can be related to the areas of small 'signal-to-noise' ratio and low coherence values. Generally the transfer function is less than or equal to 1 (or 0 dB), except for Position E, where at the higher frequencies the response at E is greater than that at Position A. This is an indication that the blade passes closest to the fuselage between Locations A and E and in fact may pass closer to E than to Location A. The lower response at the BPF for Position E is a result of the low autospectra level at Position E, see Figure 17. The magnitude of the TF changes considerably for hover, see Figure 37. In this case, many of the positions show transfer function levels of approximately 0 dB in magnitude. For these, the pressure at Positions A-H are nearly equal in magnitude. This would be expected in hover where the blades rotate nearly the same distance from all the transducers, except K. The TF for K is less than 1 (or < 0 dB).

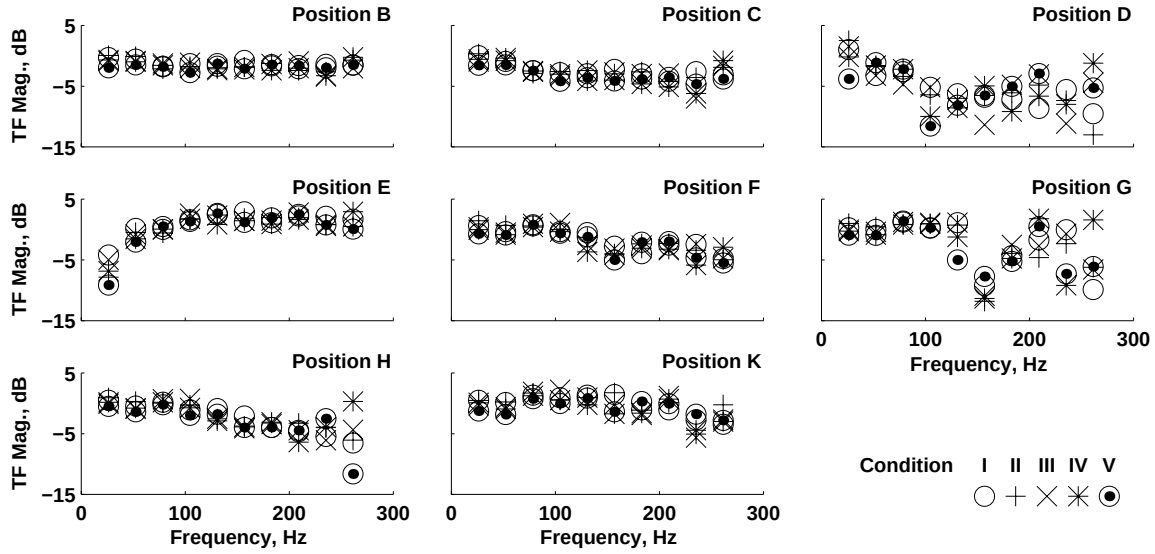

Figure 36 Transfer function magnitude for exterior pressures relative to pressure at Position A for forward flight conditions.

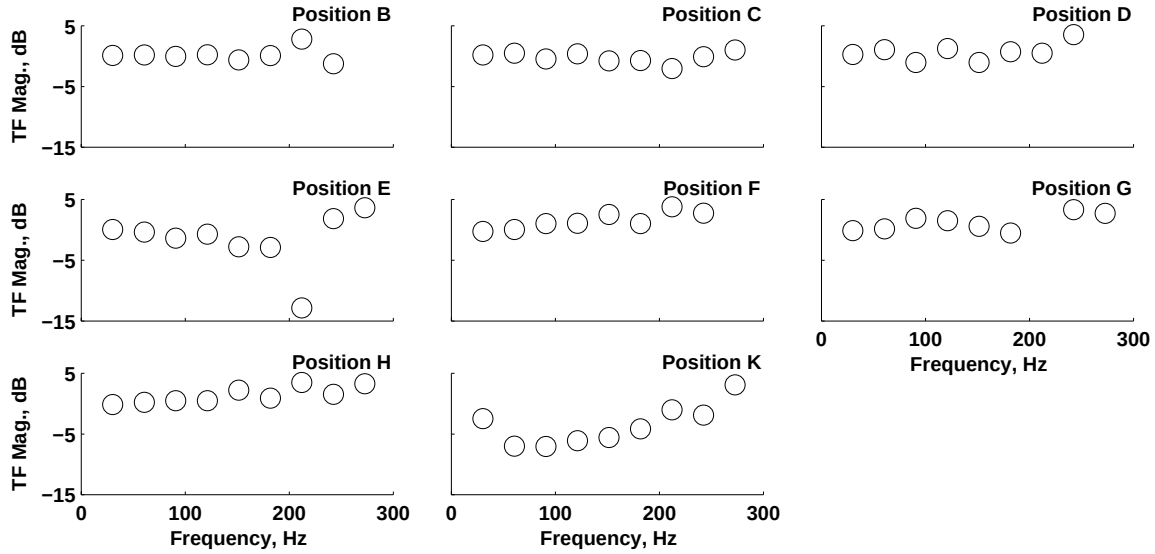

Figure 37 Transfer function magnitude for exterior pressures relative to pressure at Position A for hover.

The transfer function phase relation between the exterior positions B through K relative to the exterior pressure at position A can be used to determine the rate at which the incident pressure wave is propagating. This information can be then utilized as a means for determining how the sound waves are propagated to the fuselage surface. This is particularly important for the follow-on studies which will evaluate rotor code predictions based on this data. Details of this analysis can be found in Bendat[3]. In simplistic terms, the phase angle of the transfer function can be related to the plane pressure wave by:

$$\theta(f) = \frac{2\pi f d \cos(\phi)}{c} \times \frac{360}{2\pi}$$

where θ is the phase of the transfer function between the two surface pressure sensors (degrees), f is the frequency (Hz), d is the distance between the two sensors (m), c is the pressure wave speed (m/s), and ϕ is the angle of incident pressure wave. Differentiating this equation with respect to f results in the following expressions for the phase rate:

$$\theta'(f) = \frac{2\pi d \cos(\phi)}{c} \times \frac{360}{2\pi}$$

For plane waves which are normal to the fuselage surface, ϕ is 90 degrees and thus the TF phase rate is zero. If the plane waves are parallel to the fuselage, ϕ is 0 and the phase rate is a linear function of *f*. In order to bound the possible results, the phase rates will be assumed to fall within the area between a phase rate of 0 and that described by the preceding equation when ϕ is zero. The distance *d* (see Table I) was calculated utilizing the coordinates in the table. The speed *c* is assumed to have two different values: for locations B through D, that are not in the propeller plane, this was anticipated to be the speed of sound or 343 m/s plus the convection velocity. The average convection velocity was assumed to be that for Condition III or 92.5 m/s. The data presented in the next figures indicate that the effect of changing the actual convection velocity in forward flight (Conditions I through V) was not discernible. For sensors E through K, located in the propeller plane, the phase rate was anticipated to be related to the blade tip speed or 204.5 m/s for forward flight. In hover the pressure waves were assumed to be solely acoustic.

The measured phase rates were determined by fitting a line through the data in Figures 38 and 40. Frequencies where large scatter occurs were not included in the fitting process. Figure 39 shows the comparison between experimental and analytical phase rates. The transfer function phase rate for Positions B through D (denoted by '+') fall near the analytical "acoustic" line for grazing incidence. The accuracy of the measured phase rate for Position D is questionable due to the large data scatter. The positions which were apriori assumed to be primarily affected by blade rotation effects, E through K, are indicated by the circles. Positions G and H fall on the analytical "aerodynamics" line for grazing incidence. Position F was at the top of the aircraft and assumed to be equally influenced by both rotors. The measured phase slope in Figure 38 for Position E shows almost no variation with frequency indicating that the closest approach of the propeller is between Positions A and E. Since the response at Position E is larger than that at Position A, it could be inferred that the propeller actually passes the fuselage closer to Position E. Also from Figure 39, the pressure wave incident at Location K would be a little greater than grazing incidence (0 degrees).

A similar set of plots for hover has been included (Figures 40 and 41). For this case the analytical phase rates change sign due to the different orientation of the rotor with respect to the fuselage surface. For hover, all the positions are assumed to have acoustic waves. The phase rate at locations E, F, G, and H, see Figure 40, (these locations are on the top of the fuselage) are nearly zero over the frequency range of interest. This would indicate the exterior pressure is essentially a plane wave incident normal to the surface.

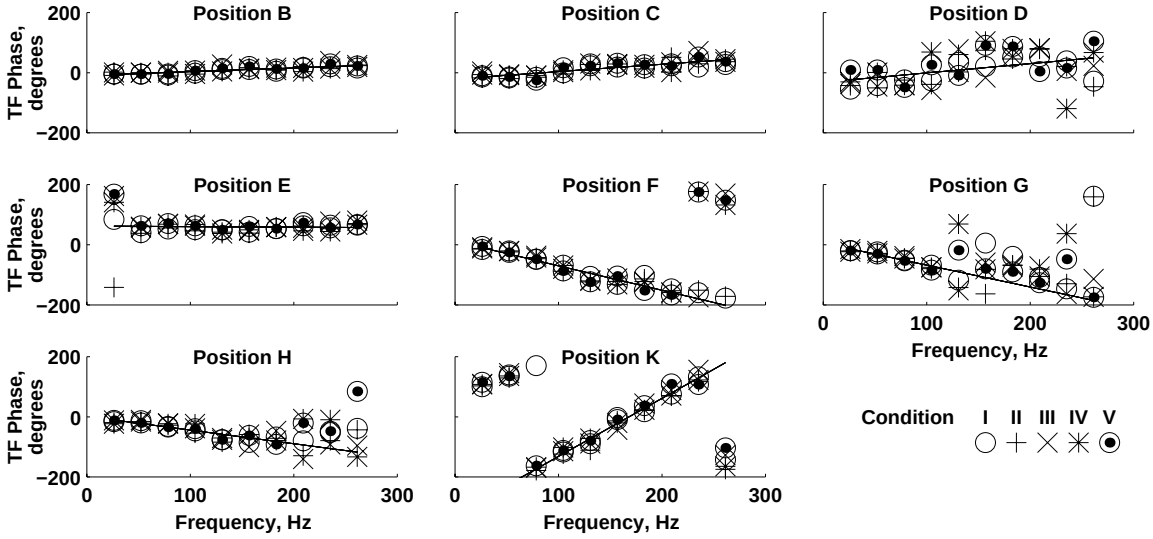

Figure 38 Transfer function phase for exterior pressures relative to Position A for forward flight.

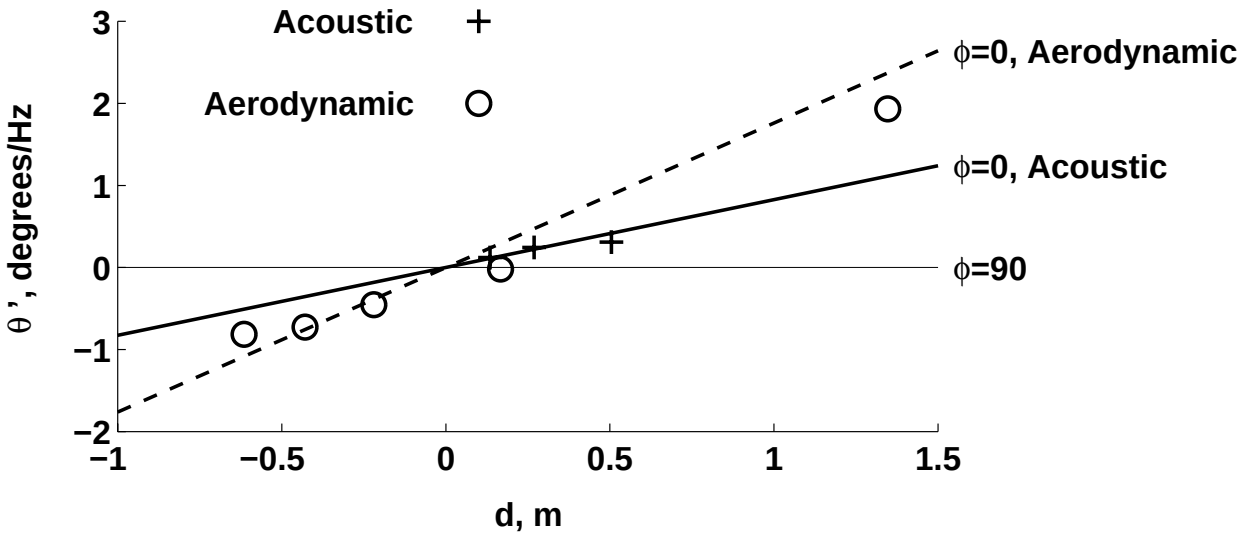

Figure 39 Comparison of analytical and measured phase rates for forward flight, see Table I for "d" values.

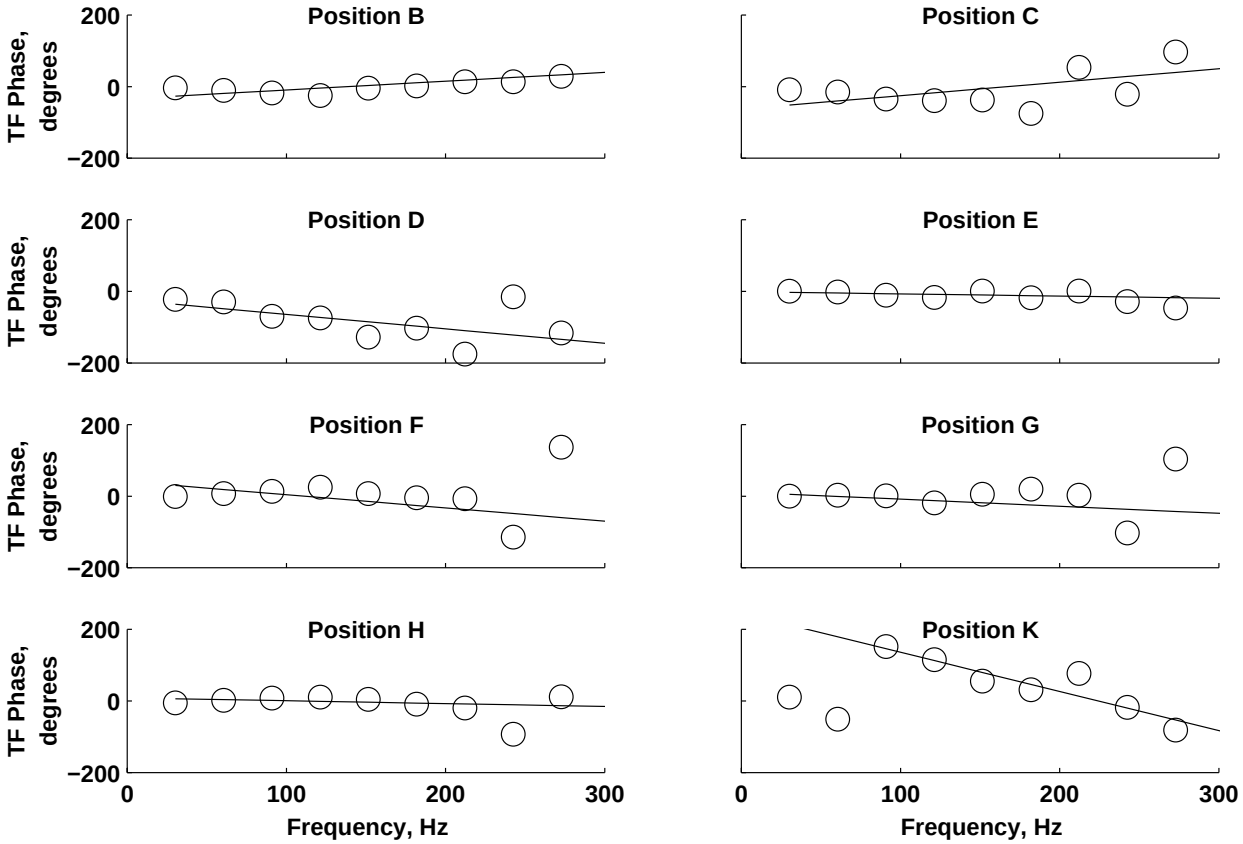

Figure 40 Transfer function phase for exterior pressures relative to Position A for hover.

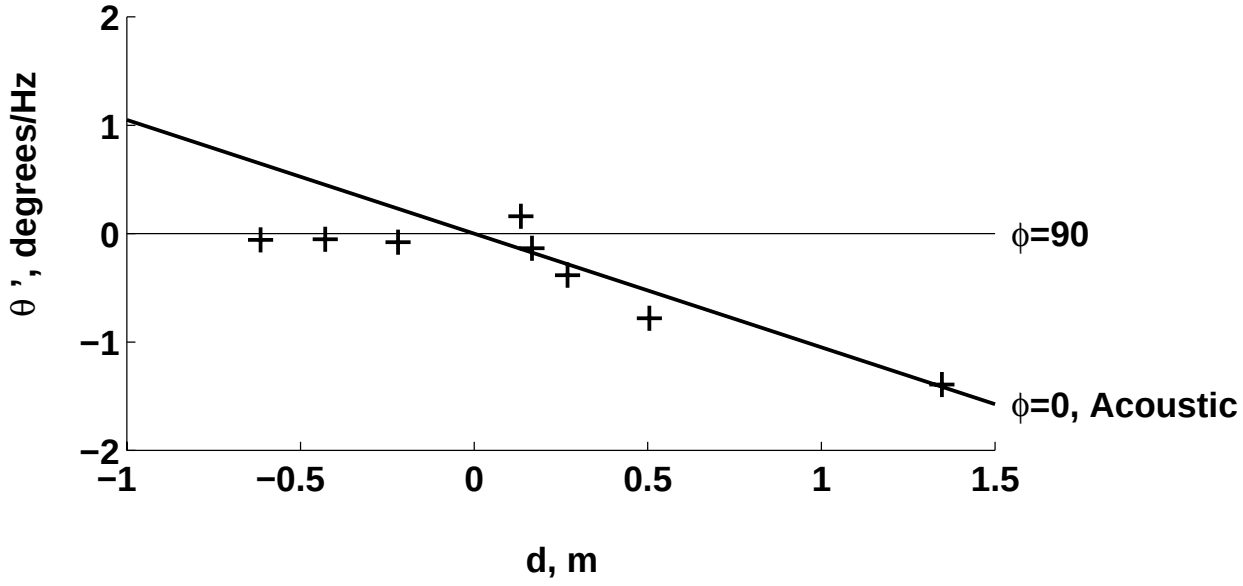

Figure 41 Comparison of analytical and measured phase rates for hover.

Mobility

The input mobilities (or inverse of impedance) at positions A, B, C, E, and H are given in Figures 42-44 for both forward flight and hover. The mobilities were based on the structural velocity (derived from the acceleration measurement) relative to the collocated exterior pressure. Sample narrowband mobility plots for Condition II are shown in Figure 42. For all cases, the mobilities at the lower frequencies are dominated by the BPF harmonics.

Below 300 Hz, the low mobility values at frequencies other than the BPF harmonics can be attributed to: 1) the very low acceleration measurements (very low signal to noise) at the lower frequencies; and 2) the exterior sensors measure significant uncorrelated pressures, while the accelerometers respond to an integrated fuselage response. Mobility values only at the harmonics up to 300 Hz based on the time averaged time histories are shown in Figures 43 and 44. The magnitude of the mobility changes very little with location, once the data with low coherence values have been eliminated.

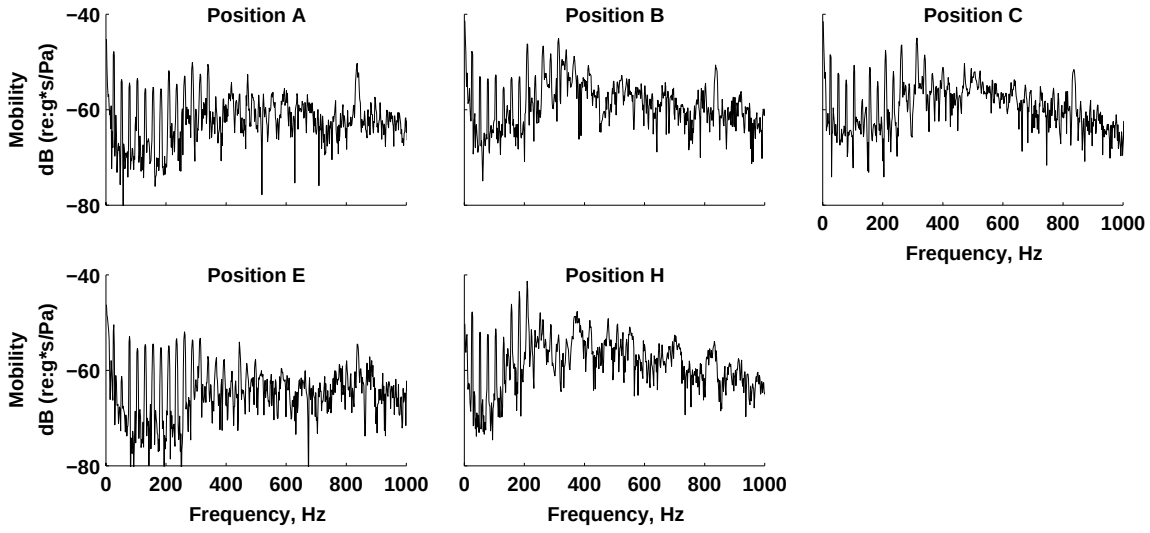

Figure 42 Sample narrowband mobility for velocities relative to exterior pressures for Condition II.

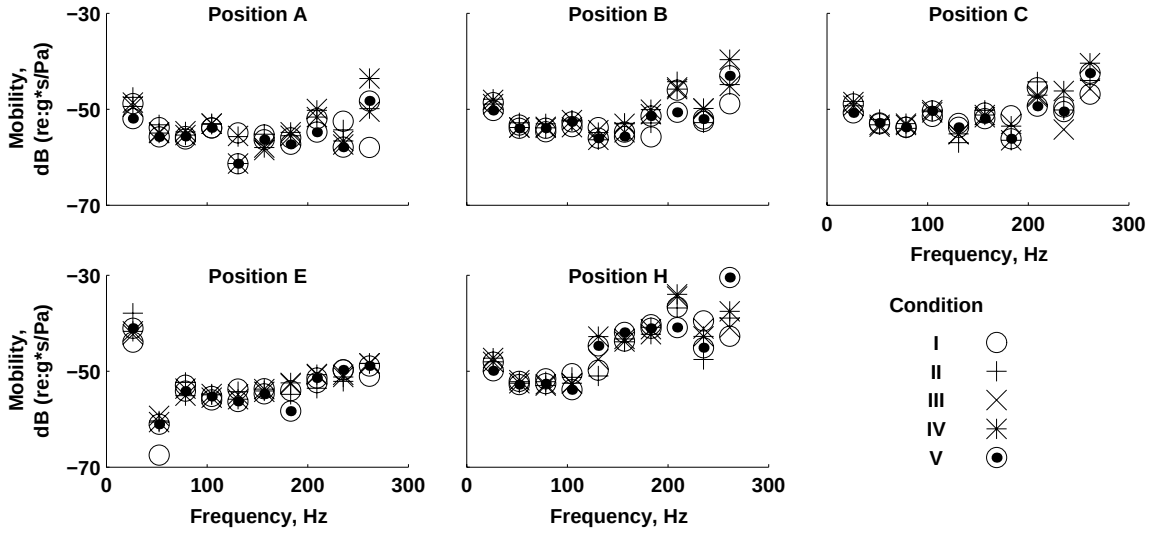

Figure 43 Mobility for velocities relative to exterior pressures for forward flight

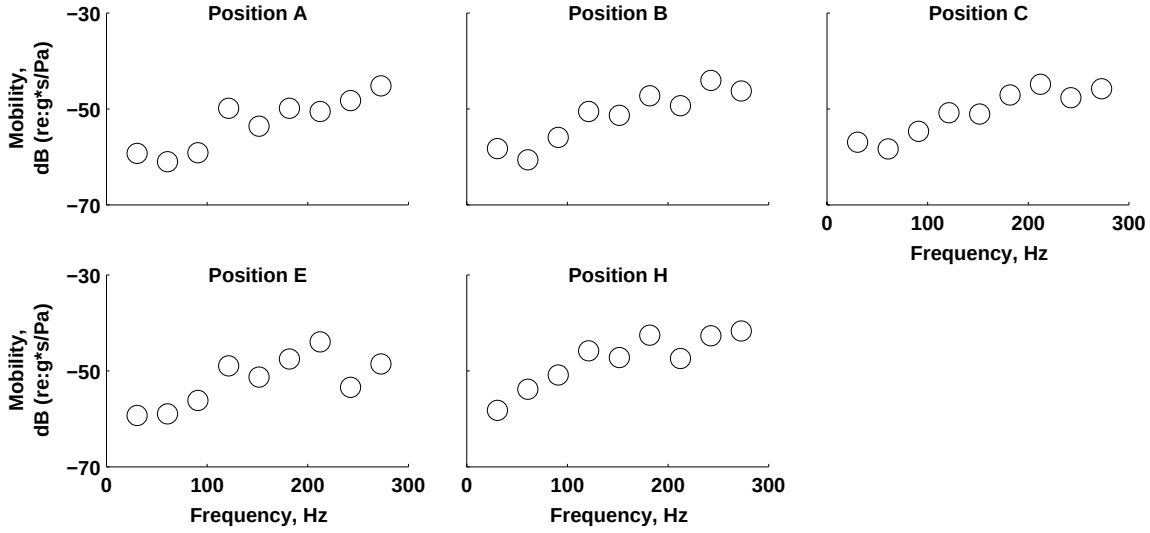

Figure 44 Mobility for velocities relative to exterior pressures for hover.

Concluding Remarks

Structural-acoustic measurements were taken aboard an XV-15 aircraft and are presented in this paper. The measurements included exterior surface pressures, structural accelerations and interior pressures. The flight conditions included both level flight in airplane mode (nacelle at 0 degrees) and out-of-ground-effect (OGE) hover in helicopter mode (nacelle at 90 degrees). For airplane mode, the speed ranged from 72 m/s to 113 m/s. The data were analyzed in both the time and frequency domains. Autospectral, coherence, and cross-spectral techniques were used. The following conclusions were drawn from the data:

1) For level flight in airplane mode, as the flight speed increased then the overall response levels increased.

2) The overall interior noise levels during hover were lower than those at the higher flight speeds for airplane mode. This was contrary to previously published results which indicated that hover levels were comparable to the higher flight speeds.

3) The flight speed did not significantly change the character of the responses, but simply increased the response levels. However, the response characteristics did vary as a function of measurement location.

4) The responses in hover were fundamentally different from those in airplane mode. For hover, the effect of measurement location on the response characteristics was small.

5) Both the exterior and interior pressures were primarily composed of responses at the BPF harmonics. The accelerations were dominated by broadband high frequency responses.

6) Coherence values could be utilized to ascertain the reliability of the spectral values at the BPF harmonics.

7) The transfer function values (both magnitude and phase) between the exterior sensors indicated that the closest approach of the effective acoustic source location of the propeller to the fuselage was at Position E.

8) The exterior sensor transfer function phase rates could be utilized to determine if the exterior pressure was primarily produced by acoustic or aerodynamic sources. This was accomplished with a simple algebraic expression.

In conclusion, the data are considered of sufficient quality to allow validation or development of a prediction code capable of accurately predicting the exterior pressure on the fuselage. These predictions will be used as input to a numerical structural-acoustic tiltrotor model. Such models can then be used to design quieter tiltrotors for the future.

---

[1] Shank, S. “Tiltrotor Interior Noise Characteristics” Proceedings American Helicopter Society/Royal Aeronautical Society Technical Specialists’ Meeting on Rotorcraft Acoustics and Rotor Fluid Dynamics, Philadelphia, PA, October 15-17, 1991.

[2] Maisal, M., principal investigator, US Army AATD, private correspondence, 1983.

[3] Bendat, J. and Piersol, A., **Engineering Applications of Correlation and Spectral Analysis**, John Wiley and Sons, 1980.